

Perovskite-Type InCoO3 with Low-Spin Co(3+): Effect of In-O Covalency on Structural Stabilization in Comparison with Rare-Earth Series

Koji Fujita, Takahiro Kawamoto, Ikuya Yamada, Olivier Hernandez, Hirofumi Akamatsu, Yu Kumagai, Fumiyasu Oba, Pascal Manuel, Ryo Fujikawa, Suguru Yoshida, et al.

▶ **To cite this version:**

Koji Fujita, Takahiro Kawamoto, Ikuya Yamada, Olivier Hernandez, Hirofumi Akamatsu, et al.. Perovskite-Type InCoO3 with Low-Spin Co(3+): Effect of In-O Covalency on Structural Stabilization in Comparison with Rare-Earth Series. Inorganic Chemistry, 2017, 56 (18), pp.11113-11122. 10.1021/acs.inorgchem.7b01426 . hal-01617946

HAL Id: hal-01617946

https://univ-rennes.hal.science/hal-01617946

Submitted on 13 Nov 2017

HAL is a multi-disciplinary open access archive for the deposit and dissemination of scientific research documents, whether they are published or not. The documents may come from teaching and research institutions in France or abroad, or from public or private research centers.

L'archive ouverte pluridisciplinaire **HAL**, est destinée au dépôt et à la diffusion de documents scientifiques de niveau recherche, publiés ou non, émanant des établissements d'enseignement et de recherche français ou étrangers, des laboratoires publics ou privés.

Perovskite-Type $InCoO_3$ with Low-Spin Co^{3+}: Effect of In–O Covalency on Structural Stabilization in Comparison with Rare-Earth Series

Koji Fujita,[†,*] Takahiro Kawamoto,[†] Ikuya Yamada,[‡] Olivier Hernandez,[§] Hirofumi Akamatsu,[∥] Yu Kumagai,[⊥] Fumiyasu Oba,[∥,⊥] Pascal Manuel,[#] Ryo Fujikawa,[†] Suguru Yoshida,[†] Masayuki Fukuda,[†] and Katsuhisa Tanaka[†]

[†]Department of Material Chemistry, Graduate School of Engineering, Kyoto University, Katsura, Nishikyo-ku, Kyoto 615-8510, Japan

[‡]Nanoscience and Nanotechnology Research Center, Osaka Prefecture University, 1-2 Gakuen-cho, Sakai, Osaka 599-8531, Japan

[§]Institut des Sciences Chimiques de Rennes, Equipe Chimie du Solide et Matériaux, UMR CNRS 6226, Université de Rennes 1, 263 Avenue du Général Leclerc, 35042 Rennes, France

[∥]Laboratory for Materials and Structures, Institute of Innovative Research, Tokyo Institute of Technology, Yokohama 226-8503, Japan

[⊥]Materials Research Center for Element Strategy, Tokyo Institute of Technology, Yokohama 226-8503, Japan

[#]ISIS Facility, STFC Rutherford Appleton Laboratory, Harwell Science and Innovation Campus, Oxon OX11 0QX, United Kingdom

Supporting Information

ABSTRACT: Perovskite rare-earth cobaltites $ACoO_3$ (A = Sc, Y, and La–Lu) have been of enduring interest for decades due to their unusual structural and physical properties associated with the spin-state transitions of low-spin Co^{3+} ions. Herein, we have synthesized a non-rare-earth perovskite cobaltite, $InCoO_3$, at 15 GPa and 1400 °C and investigated its crystal structure and magnetic ground state. Under the same high-pressure and high-temperature condition, we also prepared a perovskite-type $ScCoO_3$ with an improved cation stoichiometry compared to a previous study where the synthesis at 6 GPa and 1297 °C yielded a perovskite cobaltite with cation mixing on the A-site, $(Sc_{0.95}Co_{0.05})CoO_3$. The two perovskite phases have nearly stoichiometric cation compositions, crystallizing in the orthorhombic *Pnma* space group. In the present investigation, comprehensive studies on newly developed and well-known *Pnma* $ACoO_3$ perovskites (A = In, Sc, Y, and Pr–Lu) show that $InCoO_3$ does not fulfil the general evolution of crystal metrics with A-site cation size, indicating that $InCoO_3$ and rare earth counterparts have different chemistry for stabilizing the *Pnma* structures. Detailed structural analyses combined with first-principles calculations reveal that the origin of the anomaly for $InCoO_3$ is ascribed to the A-site cation displacements that accompany octahedral tilts; despite the highly tilted CoO_6 network, the In–O covalency makes In^{3+} ions reluctant to move from their ideal cubic-symmetry position, leading to the smaller orthorhombic distortion than expected from electrostatic/ionic size mismatch effects. Magnetic studies demonstrate that $InCoO_3$ and $ScCoO_3$ are diamagnetic with a low-spin state of Co^{3+} below 300 K, in contrast to the case of $(Sc_{0.95}Co_{0.05})CoO_3$ where the high-spin Co^{3+} ions on the A-site generate a large paramagnetic moment. The present work extends the accessible composition range of the low-spin orthocobaltite series and thus should help to establish a more comprehensive understanding of the structure–property relation.

1. INTRODUCTION

There has been increased interest in recent years in transition-metal perovskite oxides AMO_3 (M = transition metal) with unusually small A-site cations because they extends the range of existence of perovskite phases and the variety of their properties.[1,2] The A site of AMO_3 perovskites is usually occupied by large cations like alkali, alkali-earth, and rare-earth ions. The smallest typical cation occupying the A site is Lu^{3+}. When cations smaller than Lu^{3+} (e.g. Mn^{2+}, Sc^{3+}, and In^{3+} ions) are introduced into the A-sites, the perovskite structure becomes so unstable in ambient conditions that it is converted into other structures such as ilmenite-, bixbyite-, and hexagonal $LuMnO_3$-type structures.[3] The stability and structural distortions of simple perovskites are often discussed in terms of Goldschmidt tolerance factor, $t = (r_A + r_O) / (\sqrt{2}\,(r_M + r_O))$, where r_A, r_M, and r_O stand for the ionic radii of A-site, B-site and O^{2-} ions, respectively.[4] The ideal cubic perovskite has $t \sim 1$ and the incorporation of small A-site cations for which $t < 1$ leads to symmetry lowering into the orthorhombic or rhombohedral perovskite structures as a result of different tilt distortions of MO_6 octahedra. Further reduction in A-site cation size, which results in t below a limit ($t < 0.8$),[5] often gives rise to non-perovskite structures due to destabilization of otherwise

highly tilted perovskite structures. Nevertheless, it is now possible to stabilize novel perovskite compounds with extremely small t values as metastable ambient phases by utilizing high-pressure synthesis.

Among such small-tolerance factor perovskite oxides, Sc- and In-based compounds, ScMO$_3$ and InMO$_3$, and related materials have been extensively studied to find intriguing structural and magnetic properties associated with large structural distortions.[1,6–21] For example, Castillo-Martínez et al.[6] synthesized an orthorhombic $ScVO_3$ perovskite (space group *Pnma*) at 8 GPa and 800 °C and demonstrated stabilization of a rarely found tetragonal Jahn–Teller distortion at room temperature. This compound also exhibits a nontrivial spin structure at low temperatures, in contrast to *C* or *G*-type antiferromagnetic ordering for the other AVO$_3$ perovskites (A = Y and La–Lu). Belik et al.[7] prepared *Pnma* $ScCrO_3$ and $InCrO_3$ perovskites at 6 GPa and 1227 °C, and found that these compounds exhibit *C*-type antiferromagnetic ordering, contrasting with the *G*-type structure for the other ACrO$_3$ perovskites with large rare-earth ions on the A sites.[8] Although $ScMnO_3$ and $InMnO_3$ perovskites are difficult to prepare at 5–6 GPa and 800–1100 °C,[1,22–24] the high-pressure treatment over 10 GPa turns out to stabilize the perovskite phases. For $ScMnO_3$, it has been reported that the increase in pressure up to 12.5 GPa (at 1100 °C) creates a perovskite modification.[11] In the case of $InMnO_3$, the application of 10 GPa (at 1200 °C) produces a perovskite phase, but with a large amount of rhombohedral In_2O_3 impurity (~30 wt%); namely, the perovskite phase is enriched in Mn with respect to the stoichiometric composition of $InMnO_3$ and has been identified as having a cation mixing at the A-site, $(In_{1-y}Mn_y)MnO_3$.[1] $ScMnO_3$ and $(In_{1-y}Mn_y)MnO_3$ perovskites crystallize in a monoclinic ($P2_1/n$) symmetry,[1,12] which is lower than the crystal symmetry of the other AMnO$_3$ perovskites (orthorhombic *Pnma* perovskites are obtained as the stable phase for A = La–Dy or the metastable phase for A = Y and Ho–Lu). Using a high pressure above 10 GPa, we synthesized two polar rhombohedral (*R*3*c*) perovskite ferrites, $ScFeO_3$ and $InFeO_3$,[15,16] although the other AFeO$_3$ perovskites with large rare-earth ions on the A sites adopt a nonpolar orthorhombic *Pnma* perovskite structure. More generally, these *R*3*c* phases are regarded as $LiNbO_3$-type polar magnets, exhibiting room-temperature coexistence of polar structural distortion and magnetic order. *R*3*c* $ScFeO_3$ and $InFeO_3$ are thus potential candidates as magnetoelectric multiferroics.

Despite the enhanced capabilities in materials exploration through high-pressure synthesis techniques, the range of existence of perovskite cobaltites ACoO$_3$ is, on the other hand, scarcely extended toward the small-tolerance factor side. Recently, Belik et al.[17] reported the synthesis of $ScCoO_3$ under 6 GPa and 1297 °C, but with a nonstoichiometric, Co-rich composition, $Sc_{0.9}CoO_{2.85}$. The structural analysis indicated the formation of a *Pnma* perovskite with cation mixing at the A-site, $(Sc_{0.95}Co_{0.05})CoO_3$. To our knowledge, the synthesis of stoichiometric $ScCoO_3$ perovskite still remains elusive. Also, previous attempts to prepare perovskite-type $InCoO_3$ were unsuccessful under 6–7.5 GPa at elevated temperatures up to 1627 °C.[1] The scarcity of small-tolerance factor perovskite cobaltites is probably related to the inherent difficulty in stabilizing Co^{3+} ions. Indeed, even for existing perovskite cobaltites, the synthesis requires increasingly oxidizing conditions as the size of the A^{3+} ions decreases from La to Lu, and so high-pressure synthesis in the presence of an oxidizing agent (e.g., $KClO_4$) serves to obtain the compounds in single phases, especially for the smaller A^{3+} ions (A = Tm, Yb, and Lu).[25]

Here, we report the successful preparation of a small-tolerance factor perovskite $InCoO_3$ (t = 0.80) by increasing the synthesis pressure up to ~15 GPa at elevated temperature. We also show the possibility of obtaining nearly stoichiometric $ScCoO_3$ (t = 0.78) under the same high-pressure and high-temperature condition. Emphasis is placed on identifying the crystal structure and magnetic ground state of these small-tolerance factor perovskites. Early works reported that ScMO$_3$ and InMO$_3$ perovskites with early 3d-transition metals (M = V, Cr, and Mn) crystallize in orthorhombic (*Pnma*) or monoclinic ($P2_1/n$) symmetries,[6–12] while the rhombohedral symmetry (*R*3*c*) appears for the middle 3d-transition metal (M = Fe).[15,16] Hence, it is interesting to examine which crystal structure type is stabilized for the later 3d-transition metals such as Co. The spin state of Co^{3+} ions is another important aspect. A series of perovskite cobaltites, ACoO$_3$ (A = Y and La–Lu), has received continued attention for decades because they exhibit a degree of freedom in the electronic configuration of Co^{3+} ions, in addition to the spin, charge, and orbital degrees of freedom. All the members of the series have a low-spin ground state of Co^{3+} ions ($t_{2g}^6e_g^0$, S = 0). With increasing temperature, they undergo two magnetic transitions associated with thermal excitations to either the intermediate-spin ($t_{2g}^5e_g^1$, S = 1) or high-spin ($t_{2g}^4e_g^2$, S = 2); although the nature of paramagnetic Co^{3+} species is still under debate, the first magnetic transition is ascribed to the diamagnetic-paramagnetic transition,[26–29] and the second one to the transition to another paramagnetic state accompanied by an insulator-metal transition.[30–34] Given the fact that $(Sc_{0.95}Co_{0.05})CoO_3$ exhibits a large paramagnetic response from the high-spin Co^{3+} ions on the A-site,[17] the magnetic ground states of almost stoichiometric $ScCoO_3$ and $InCoO_3$ deserve to be investigated to confirm a link with the well-known members of the perovskite cobaltite series.

Our characterizations show that $ScCoO_3$ and $InCoO_3$ obtained here expand the accessible composition range of the low-spin orthocobaltite series, unlike the case of $(Sc_{0.95}Co_{0.05})CoO_3$.[17] In this work, a comprehensive comparison of crystal structure is also made for newly developed and well-known orthocobaltites ACoO$_3$ (A = In, Sc, Y, and Pr–Lu). We find that $InCoO_3$ does not follow the general evolution of crystal metrics with A-site cation size, implying that $InCoO_3$ and rare earth counterparts (A = Sc, Y, and Pr–Lu) have a distinct chemistry to stabilize the orthorhombic structures. The origin of such a peculiarity for $InCoO_3$ is argued with help of first-principles calculations.

2. EXPERIMENTAL AND COMPUTATIONAL DETAILS

Polycrystalline $InCoO_3$ and $ScCoO_3$ were synthesized by the solid-state reaction under high-pressure and high-

temperature conditions in the presence of $KClO_4$ as an oxidizing agent. Reagent-grade In_2O_3 (99.999 %, Kojundo Chemical), Sc_2O_3 (99.9%, Kojundo Chemical), Co_3O_4 (99.9 %, Kojundo Chemical) and $KClO_4$ (99.99 %, Sigma-Aldrich) were used as starting materials. A_2O_3 (A = Sc or In), Co_3O_4, and $KClO_4$ were mixed in a molar ratio of 1.5 : 1 : 0.225 in an agate mortar. The resultant mixture was placed into a Pt capsule and put into a high-pressure cell. The solid-state reaction was performed at 15 GPa and 1400 ºC for 30 min using a Kawai-type high-pressure apparatus, followed by a rapid temperature quench and then a gradual pressure release. The obtained sample was washed with water, ethanol, and acetone several times to remove KCl.

Synchrotron X-ray diffraction (SXRD) data were recorded at 300 K on the BL02B2 beamline at SPring-8 equipped with a large Debye-Scherrer camera using monochromated X-rays (λ = 0.65084 or 0.77475 Å). The minimum d value reached was as low as 0.524 Å. The powder sample was loaded into a Lindemann glass capillary with an inner diameter of 0.1 mm ($InCoO_3$) or 0.2 mm ($ScCoO_3$), which was continuously rotated during the measurement to reduce the effect of preferential orientation. The time-of-flight (TOF) neutron powder diffraction (NPD) was carried out for $ScCoO_3$ at room temperature using the WISH diffractometer at ISIS neutron facility.[35] Approximately 40 mg of sample powders was housed in a vanadium can. Bank 4 at 2θ = 121.7° was used for the refinement, allowing us to cleanly catch the observable Bragg reflections in the d range of 0.63 to 4.05 Å with a high resolution and a satisfactory counting statistics despite the small sample volume. All the structural refinements were carried out through the Rietveld method[36] using the FullProf program.[37] An absorption correction was made during the Rietveld refinements against the SXRD data,[38] μr values of 0.36 and 0.70 were used for $InCoO_3$ and $ScCoO_3$, respectively. For the TOF NPD data, a cylindrical sample absorption correction was also applied. The crystal structure was drawn by the program VESTA.[39] The cation ratio was evaluated with electron probe microanalysis (EPMA) using a JEOL JXA-8500F instrument. Sc_2O_3, In_2O_3, and Co_3O_4 were utilized as standard samples. The magnetic susceptibility data were recorded using a SQUID magnetometer (MPMS-XL; Quantum Design) between 5 and 300 K under an applied field of 100 Oe.

To explore comparatively the crystal and electronic structures of $InCoO_3$ and $ScCoO_3$ against their isostructural analogues $ACoO_3$ (A = Y and Pr–Lu), we used DFT calculations. As a reference, calculations were also made for as-yet unsynthesized $TlCoO_3$. Our first-principles calculations were carried out using the projector augmented-wave (PAW) method[40] as implemented in the VASP code.[41–45] The exchange-correlation interactions among electrons were treated by using the HSE06 hybrid functional,[46–48] which is shown to predict appropriately the magnetic, electronic, and structural properties in insulating transition metal compounds.[49–54] The PAW data sets with radial cutoffs of 1.6 Å for Pr, Nd, Sm, Gd, Tb, Dy, Ho, Er, Tm, and Lu, and Sc; 1.7 Å for Eu, Yb, In, and Tl; 1.8 Å for Y and Ce; 1.3 Å for Co; and 0.8 Å for O were used with a plane-wave cutoff energy of 550 eV. The following states were described as valence electrons: 3s, 3p, 3d, and 4s for Sc; 4s, 4p, 4d, and 5s for Y; 5s, 5p, 5d, and 6s for Ce, Pr, Nd, and Sm; 5p, 5d, and 6s for Eu, Gd, Tb, Dy, Ho, Er, Tm, Yb, and Lu; 4d, 5s, and 5p for In; 5d, 6s, and 6p for Tl; 3s, 3p, 3d, 4s for Co; and 2s and 2p for O. A 3 × 2 × 3 k-point mesh was used for the *Pnma* unit cell with 20 atoms, in accordance with the Monkhorst-Pack scheme.[55] A diamagnetic ground state was assumed according to the present and previous works.[27–29,32–34] The lattice constants and internal coordinates were fully optimized in each case until the residual stresses and forces converged to less than 0.5 GPa and 0.05 eV/Å, respectively.

3. RESULTS

3.1. Crystal Structure: **Figure 1a** and **b** show the SXRD data at 300 K for $InCoO_3$ and $ScCoO_3$, respectively, together with the results of their Rietveld refinements. For each of the data sets, the main reflections can be indexed in orthorhombic symmetry with a $\sqrt{2}a_p \times 2a_p \times \sqrt{2}a_p$ unit cell (where a_p is the lattice parameter of basic cubic perovskite).

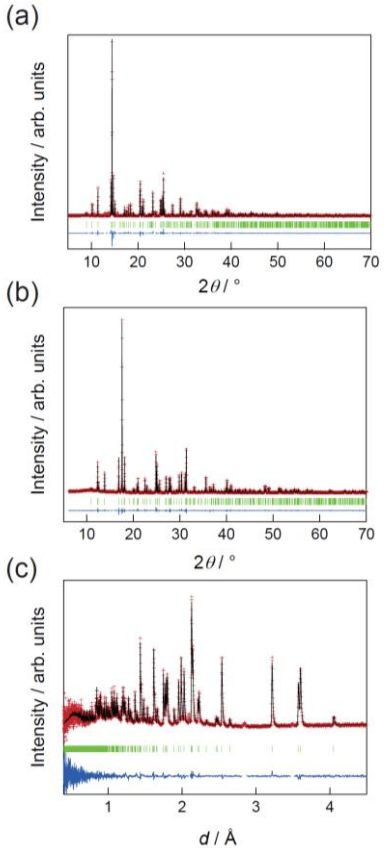


Figure 1. Rietveld refinements against SXRD data at 300 K for (a) $InCoO_3$ (λ = 0.65084 Å) and (b) $ScCoO_3$ (λ = 0.77475 Å) and (c) Rietveld refinement against TOF NPD data at 300 K for $ScCoO_3$ (bank 4 at 2θ = 121.7°). These refinements are performed on the basis of the orthorhombic (*Pnma*) perovskite-type structure, showing the observed (crosses) and calculated (solid line) profiles. The bottom solid line represents the difference between the observed and calculated profiles. The ticks correspond to the positions of the calculated Bragg reflections for *Pnma* perovskite cobaltites. The unindexed peaks from unknown impurities were excluded from the refinement.

In contrast to the case of $(Sc_{0.95}Co_{0.05})CoO_3$ prepared at 6 GPa and 1297 °C,[17] no reflections from bixbyite-type Sc_2O_3 are found in the SXRD pattern for $ScCoO_3$. Instead, a few weak reflections from unknown phases are observed; the intensities of impurity reflections were less than 0.8 % of the intensities of the most intense perovskite reflections (**Figure S1** in the Supporting Information,). The SXRD pattern for $InCoO_3$ also contained impurity reflections at a similar level (see **Figure S1**).

Rietveld refinements were performed against the SXRD patterns for the main perovskite phase by assuming as an initial model the *Pnma* structure of $LuCoO_3$;[25] *A* (= In or Sc), Co, O1, and O2 atoms are placed at 4*c* (*x*, 1/4, *z*), 4*b* (0, 0, 1/2), 4*c* (*x*, 1/4, *z*), and 8*d* (*x*, *y*, *z*), respectively. For both compounds, the cation sites were refined anisotropically, while the anion sites were handled isotropically. For $InCoO_3$, the U_{iso} values of O1 and O2 sites were fixed to the same least-squares parameter. Since no apparent vacancy was observed at any cation sites within the limits of standard uncertainties, the occupancy factor *g* was constrained to unity. The stoichiometric composition models immediately provide good overall fits to the observed patterns for both $InCoO_3$ (weighted profile *R*-factor, R_{wp} = 11.7%, and Bragg *R*-factor, R_B = 4.52%) and $ScCoO_3$ (R_{wp} = 12.2% and R_B = 3.14%). For $ScCoO_3$, SXRD alone may not be sufficient to reliably estimate the site occupancies because of the relatively close X-ray scattering factors between Sc and Co atoms. Hence, we measured TOF NPD at 300 K to take advantage of distinct scattering lengths of Sc (1.2290×10^{-15} m) and Co (0.2490×10^{-15} m) but also to obtain more relevant values of the oxygen occupancies. **Figure 1c** shows the TOF NPD Rietveld plot for $ScCoO_3$ at 300 K. Again, the fully stoichiometric *Pnma* model leads to a satisfactory refinement (R_{wp} = 8.45% and R_B = 6.25%). The cation and anion site occupancies were refined to check deviations in the stoichiometry, but the refined occupancies were consistently within 1 or 2% of the expected values.

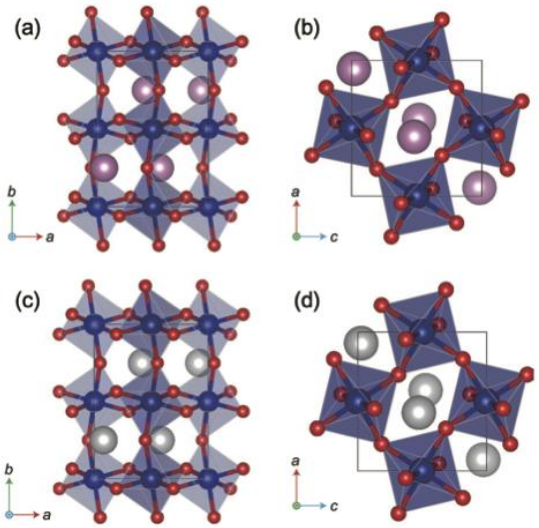


Figure 2 Crystal structures of $InCoO_3$ in (a) *ab* plane and (b) *ac* plane and those of $ScCoO_3$ in (c) *ab* plane and (d) *ac* plane. Pink, grey, blue, and red spheres represent In, Sc, Co, and O atoms, respectively.

We also checked the possibility of cation mixing on the *A*-site, according to the previous report of high-pressure synthesized $(Sc_{0.95}Co_{0.05})CoO_3$.[17] In refinements against SXRD data for $InCoO_3$, the introduction of a small content of Co (a few %) at the In 4*c* site did not improve the fitting quality. Similar results were obtained for $ScCoO_3$ when considering Co mixing on the Sc 4*c* site in the combined refinement performed simultaneously against SXRD data and TOF NPD data. Complementary EPMA on $ScCoO_3$ and $InCoO_3$ showed In/Co = 1.010(7) and Sc/Co = 0.986(8), respectively. Thus, we conclude that *Pnma* $InCoO_3$ and $ScCoO_3$ synthesized at 15 GPa and 1400 °C are almost stoichiometric within experimental standard uncertainties.

Figure 2 displays the refined crystal structures for $InCoO_3$ and $ScCoO_3$. The refinement results including the crystallographic data are listed in **Table 1**, and the selected

Table 1. Refined Structural Parameters (Atomic Coordinates and Atomic Displacement Parameters) at 300 K for Perovskite-Type $InCoO_3$ (SXRD data) and $ScCoO_3$ (SXRD and TOF NPD data)[a]

Atom	Site	*x*/*a*	*y*/*b*	*z*/*c*	U_{eq} or U_{iso} (Å^2)
			$InCoO_3$ (SXRD)		
In[†]	4*c*	0.06232(8)	1/4	0.98129(9)	0.0035
Co[†]	4*b*	0	0	1/2	0.0026
O1	4*c*	0.4478(8)	1/4	0.1182(7)	0.0012(5)
O2	8*d*	0.3021(6)	0.0613(4)	0.6937(6)	0.0012(5)
			$ScCoO_3$ (SXRD)		
Sc[†]	4*c*	0.08075(15)	1/4	0.9738(2)	0.0033
Co[†]	4*b*	0	0	1/2	0.0018
O1	4*c*	0.4484(5)	1/4	0.1292(6)	0.0023(7)
O2	8*d*	0.3057(4)	0.0648(3)	0.6837(4)	0.0024(5)
			$ScCoO_3$ (TOF NPD)		
Sc	4*c*	0.08124(16)	1/4	0.97393(19)	0.0262(3)
Co	4*b*	0	0	1/2	0.0081(10)
O1	4*c*	0.4500(3)	1/4	0.1309(3)	0.0160(5)
O2	8*d*	0.3078(2)	0.06381(16)	0.6842(2)	0.0178(4)

[a]Space group: Orthorhombic *Pnma* (No. 62), *Z* = 4. The occupancy parameter *g* is fixed to unity for all atoms. [†]Refined anisotropically. $InCoO_3$ (f.w. = 221.75 g mol^{-1}): SXRD (λ = 0.65084 Å, 0.494 Å < *d* < 7.372 Å); *a* = 5.264382(17) Å, *b* = 7.33374(2) Å, *c* = 5.076713(17) Å, and *V* = 195.9998(11) Å^3; R_{wp} = 11.70 %, R_p = 9.44%, and χ^2 = 5.31. $ScCoO_3$ (f.w. = 151.89 g mol^{-1}): SXRD (λ = 0.77475 Å, 0.599 Å < *d* < 7.280 Å); *a* = 5.284874(16) Å, *b* = 7.14173(2) Å, *c* = 4.915136(17) Å, and *V* = 185.5126(10) Å^3; R_{wp} = 12.20%, R_P = 12.1%, and χ^2 = 0.91. $ScCoO_3$ (f.w. = 151.89 g mol^{-1}): TOF NPD (0.350 Å < *d* < 5.848 Å); *a* = 5.29250(10)Å, *b* = 7.15286(14) Å, *c* = 4.92243(9) Å, and *V* = 186.346(6) Å^3; R_{wp} = 8.45 %, R_P = 28.8%, and χ^2 = 2.04. $R_{wp} = [\Sigma w_i (y_{io} - y_{ic})^2 / \Sigma w_i y_{io}^2]^{1/2}$ and $R_p = \Sigma |y_{io} - y_{ic}| / \Sigma y_{io}$, where y_{io} and y_{ic} are the observed and calculated intensities, respectively, and w_i is the weighting factor.

Table 2. Selected Bond Lengths and Bond Angle Obtained from Refinements against SXRD Data at 300 K

$InCoO_3$		$ScCoO_3$	
In–O1 / Å	3.309(4)	Sc–O1 / Å	3.428(3)
In–O1 / Å	3.103(4	Sc–O1 / Å	3.045(3)
In–O1 / Å	2.145(4)	Sc–O1 / Å	2.088(3)
In–O1 / Å	2.121(4)	Sc–O1 / Å	2.073(3)
In–O2 (×2) / Å	3.408(3)	Sc–O2 (×2) / Å	3.473(2)
In–O2 (×2) / Å	2.624(3)	Sc–O2 (×2) / Å	2.545(2)
In–O2 (×2) / Å	2.375(3)	Sc–O2 (×2) / Å	2.279(2)
In–O2 (×2) / Å	2.140(3)	Sc–O2 (×2) / Å	2.112(2)
Co–O1 (×2) / Å	1.9486(12)	Co–O1 (×2) / Å	1.9145(10)
Co–O2 (×2) / Å	1.925(3)	Co–O2 (×2) / Å	1.920(2)
Co–O2 (×2) / Å	1.923(3)	Co-O2 (×2) / Å	1.908(2)
Co–O1–Co / °	140.40(5)	Co–O1–Co / °	138.48(5)
Co–O2–Co / °	143.71(13)	Co–O2–Co / °	141.06(9)

bond lengths and bond angles are given in **Table 2**. The structural views along [101] and [010] directions show a $GdFeO_3$-type orthorhombic distortion, being characterized by $a^-b^+a^-$ tilt system in Glazer's notation.[56] As expected from the small tolerance factors, both compounds possess a notable magnitude of CoO_6 octahedral tilts, with the Co–O1–Co and Co–O2–Co angles deviating significantly from the ideal value of 180° by up to ~ 42° (see **Table 2**).

Bond valence sum (BVS) calculations[57] using the structural parameters refined from SXRD data give values of +2.964(11) and +2.703(8) for In and Co, respectively, confirming an ionic model of $In^{3+}Co^{3+}O_3$. The BVS of Sc and Co for $ScCoO_3$ [Sc = +2.982(8) and Co = +2.838(6)] are also close to the formal oxidation states expected from $Sc^{3+}Co^{3+}O_3$. The CoO_6 octahedral distortion is estimated by using the following equation: $\Delta = 1/6\sum_i[(d_i - \langle d\rangle)/\langle d\rangle]^2$, where d_i is the individual Co–O bond length, and $\langle d\rangle$ is the average Co–O bond length. We obtained $\Delta = 2.1 \times 10^{-5}$ and 4.7×10^{-5} for CoO_6 octahedra in $InCoO_3$ and $ScCoO_3$, respectively. These distortions are comparable to those observed for other perovskite cobaltites with small *A*-site cations (e.g., $\Delta = 5.53 \times 10^{-5}$ for $LuCoO_3$),[25] but are approximately two orders of magnitude lower than what has been observed for perovskite manganites $AMnO_3$ (*A* = Sc, Y, and Pr–Er) with Jahn–Teller active Mn^{3+} ions (Δ = 4.3–4.9 10^{-3}).[11,58] The very small dispersions in Co–O bonds for $InCoO_3$ and $ScCoO_3$ are ascribed to the Jahn–Teller inactive, low-spin Co^{3+} ions as mentioned below.

Here, it should be noted that the calculated density for $ScCoO_3$ (5.44 g/cm^3) in this study (15 GPa and 1400 °C) is slightly lower than that for the isostructural $(Sc_{0.95}Co_{0.05})CoO_3$ (5.47 g/cm^3) synthesized at 6 GPa and 1297 °C,[17] implying differences in the cation arrangement and stoichiometry between the two compounds. We also find that the unit-cell volume of $ScCoO_3$ (V = 185.512(2) Å^3) obtained by the combined refinement against SXRD and TOF NPD data (**Table S1** in the Supporting Information) is slightly larger than that of $(Sc_{0.95}Co_{0.05})CoO_3$ (V = 185.141 Å^3) and more comparable to that of $ScAlO_3$ (V = 185.915 Å^3).[59] This result is consistent with the fact that the 6-fold coordinated ionic radii of Co^{3+} (0.545 Å for low-spin configuration) and Al^{3+} (0.535 Å) are very close to each other,[60] validating the stoichiometric composition model for $ScCoO_3$.

3.2. Relation between Lattice Parameters and *A*-site Cation Size: $InCoO_3$ and $ScCoO_3$ adopt the same orthorhombic (*Pnma*) structure as well-studied perovskite cobaltites $ACoO_3$ (*A* = Y and Pr–Lu);[25,27,28,32–34,61] $LaCoO_3$ is excluded from the series of orthocobaltites because of the $R\bar{3}c$ symmetry.[26] Here, we examine comprehensively the evolution of structural distortions across the isostructural series of $ACoO_3$ (*A* = In, Sc, Y, and Pr–Lu). The orthorhombic lattice parameters are plotted in **Figure 3a** as a function of A^{3+} ionic radius, r_A, in 8-fold coordination.[60] $ScCoO_3$ and $InCoO_3$ both possess the orthorhombic distortion with the following relationship between lattice

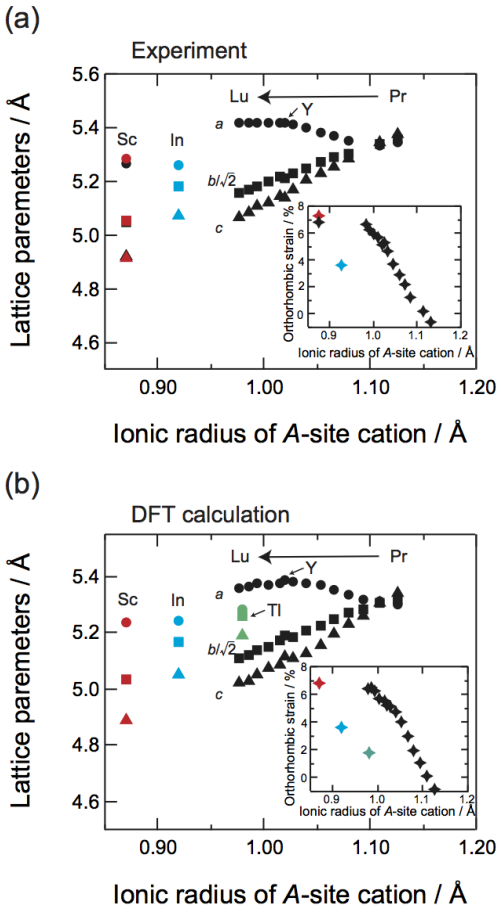


Figure 3. Variations in (a) experimental and (b) calculated lattice parameters with A^{3+} ionic radius, r_A (in 8-fold coordination[60]) for $ScCoO_3$ (red), $InCoO_3$ (blue), and $ACoO_3$ where *A* = Y and Pr–Lu (black).[25,32–34] In (a), the experimental lattice parameters for $(Sc_{0.95}Co_{0.05})CoO_3$ (black) are displayed for comparison.[17] In (b), the calculated lattice parameters for $TlCoO_3$ (green) are shown as a reference. Insets depict the r_A-dependent variations in (a) experimental and (b) calculated orthorhombic strain, $s = 2(a - c)/(a + c)$.

parameters, $c < b/\sqrt{2} < a$, which is the same as that for the other $ACoO_3$ perovskites with small A-site cations (A = Y and Sm–Lu). This kind of orthorhombic distortion is characteristic of the so-called O-type structure where the CoO_6 octahedral tilts are the dominant source of the orthorhombic distortion; the strong contractions in c accompanying the octahedral tilts eventually results in the structures with $c < a$.[62] **Figure 3a** also indicates that the relation between lattice parameters changes into $a < b/\sqrt{2} < c$ when A = Nd and Pr. The relation $a < c$ has been seen for some *Pnma* perovskites with large A-site cations, such as $PrNiO_3$ and $LaCrO_3$,[63,64] and this is ascribable to local distortions in the MO_6 octahedra (specifically, slight deviation of the O–M–O bond angles in the ac plane from 90 °), which lead to an expansion in c and a contraction in a. For $NdCoO_3$ and $PrCoO_3$, the O–Co–O bond angles are 90 ± β °, where β is about 1 °, and the β value is large enough to override the impact of the modest octahedral tilts on the relative a/c dimention.[65]

The evolution of lattice parameters (a, b, and c) across the well-studied series of $ACoO_3$ (A = Y and Pr–Lu), as shown in **Figure 3a**, is a commonly observed feature of the octahedral framework in $a^-b^+a^-$ tilt pattern, where a reduction in r_A gives rise to monotonic decreases in b and c, while leaving a almost unchanged. When the variation in lattice parameters is extrapolated toward the smaller r_A, one can see different behavior between $ScCoO_3$ and $InCoO_3$. $ScCoO_3$ approximately follows the relationship between r_A and lattice parameters found for A = Y and Pr–Lu, while this does not hold for $InCoO_3$, i.e., $InCoO_3$ displays significant deviations of all the lattice parameters from the extrapolated values at r_{In}. The r_A-dependent variation in orthorhombic strain, $s = 2(a - c)/(a + c)$, also shows a clear anomaly for $InCoO_3$ (see the inset of **Figure 3a**). The orthorhombicity for $InCoO_3$ is much smaller than the expected value from the trend for the other members of this series.

Across the isostructural series of $ACoO_3$ (A = In, Sc, Y, and Pr–Lu), the unit-cell volume decreases nearly monotonically with decreasing r_A (**Figure 4a**), suggesting a smooth increase in octahedral tilts. We estimated the tilt angles from the oxygen atomic positions by the method of Kennedy *et al.*,[66] as implemented in a previous study. The in-phase ($a^0b^+a^0$) and out-of-phase ($a^-b^0a^-$) tilt angles as well as the average tilt angle are plotted in **Figure 4b** against r_A. As expected, the average tilt angle increases roughly proportionally to the decrease in r_A, but the individual tilt angles for $InCoO_3$ deviate from the trend for the other members of this series, reflecting the anomalies in the crystal metrics as shown in **Figure 3**.

To obtain an insight into the aforementioned anomalous behavior of the crystal metrics of $InCoO_3$, we performed DFT calculations. **Figure 3b** and the inset plot the calculated orthorhombic lattice parameters and orthorhombic strain as a function of r_A, respectively. As a reference, the calculated data for an as-yet unsynthesized *Pnma* orthocobaltite, $TlCoO_3$, are also shown in these figures. The HSE06 optimized lattice parameters for each compound are almost consistent with the experimental data, and the evolution of the calculated lattice parameters and orthorhombic strain with r_A also reproduces well the experimental trend, highlighting the anomalies for $InCoO_3$. Interestingly, such anomalies are found for $TlCoO_3$ as well. These results suggest the different chemistry of group 13 (In and Tl) vs group 3 (rare earth) ions with respect to the stabilization of *Pnma* perovskites. Similar phenomena have been experimentally observed for $InCrO_3$ and $TlCrO_3$ in the orthochromite $ACrO_3$ series (A = Tl, In, Y, and La–Lu)[7,67] and for $TlFeO_3$ in the orthoferrite $AFeO_3$ series (A = Tl, Y, and Pr–Lu).[68] These previous studies considered the relatively high electronegativity of In and Tl compared to rare earth elements and suggested that the covalency of In–O and Tl–O bonds is responsible for the observed anomalies. Further discussion about the electronic effects of A-site cations on orthorhombic distortions is given in Section 4.

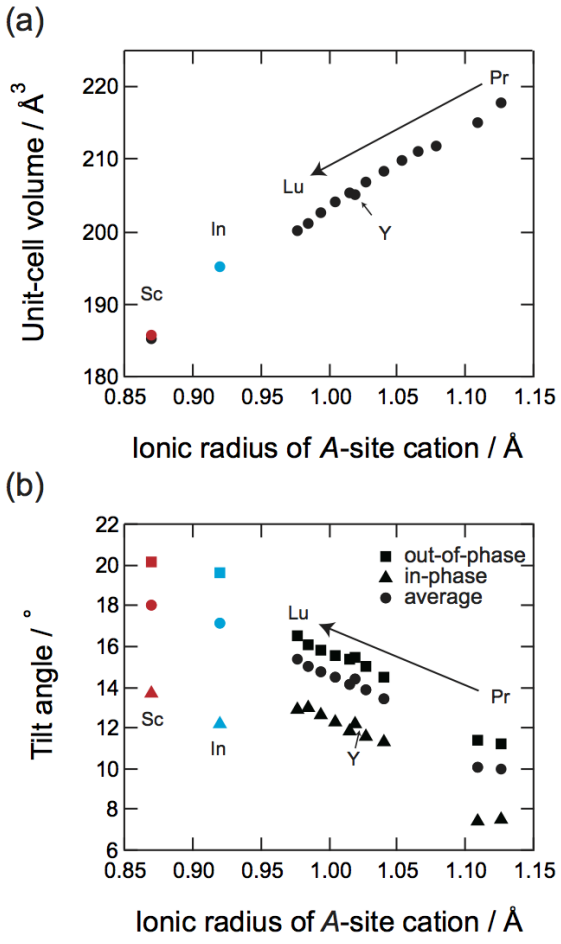


Figure 4 (a) Variations in unit-cell volume with A^{3+} ionic radius, r_A (in 8-fold coordination[60]) for $ScCoO_3$ (red), $InCoO_3$ (blue), and $ACoO_3$ where A = Y and Pr–Lu (black).[25,32–34] The unit-cell volume for $(Sc_{0.95}Co_{0.05})CoO_3$ (black)[17] is also displayed for comparison.[17] (b) Variation in octahedral tilt angles with A^{3+} ionic radius, r_A (in 8-fold coordination[60]) for $ScCoO_3$ (red), $InCoO_3$ (blue), and $ACoO_3$ where A = Y, Pr, Nd, and Tb–Lu (black).[25,32–34] The in-phase ($a^0b^+a^0$) and out-of-phase ($a^-b^0a^-$) tilt angles as well as the average tilt angle were calculated from the oxygen fractional coordinates by the equations given in ref. 66.

3.3. Magnetic Properties: **Figure 5** shows the temperature dependence of magnetic susceptibility, $\chi(T)$, of *Pnma* $ScCoO_3$ and $InCoO_3$ measured at 100 Oe after zero-field cooling. As the temperature is decreased, χ gradually increases. We analyzed the χ-T curve in the temperature range of 5 to 300 K by using the Curie-Weiss law with the equation:

$$\chi(T) = \chi_0 + \frac{N\mu_{\text{eff}}^2}{3k_B(T-\theta_w)},$$

where χ_0 is a temperature-independent term, N is the Avogadro constant, μ_{eff} is an effective magnetic moment, k_B is the Boltzmann constant, θ_w is the Weiss temperature. The fitting yields χ_0 = 4.98(2) × 10^{-3} emu Oe^{-1} mol^{-1}, θ_w = –0.2(1) K, and μ_{eff} = 0.72(3) μ_B for $InCoO_3$ and χ_0 = 1.95(2) × 10^{-4} emu Oe^{-1} mol^{-1}, θ_w = –0.72(7) K, and μ_{eff} = 0.10(1) μ_B for $ScCoO_3$. The effective magnetic moments are much smaller than those for intermediate-spin state Co^{3+} (2.828 μ_B) and high-spin state Co^{3+}(4.899 μ_B). This, together with the very weak magnetic interactions (θ_w ~ 0 K), suggests that the paramagnetic contributions stem from magnetic impurities and/or from a very small amount of defects in the structure. It should be mentioned that the present situation is quite different from that for $(Sc_{0.95}Co_{0.05})CoO_3$ prepared at 6 GPa and 1297 °C, where the cation mixing on the *A*-site leads to the larger magnetic moment and stronger magnetic interaction (μ_{eff} = 1.749 μ_B and θ_w. = −130 K).[17] The large effective moment for $(Sc_{0.95}Co_{0.05})CoO_3$ is ascribed to the presence of high-spin Co^{3+} ions on the *A*-site, while the *B*-site Co^{3+} ions have a low-spin configuration. Given the nearly stoichiometric compositions of the present $ScCoO_3$ and $InCoO_3$, it is reasonable to conclude that their magnetic ground state is diamagnetic with a low-spin state of Co^{3+}.

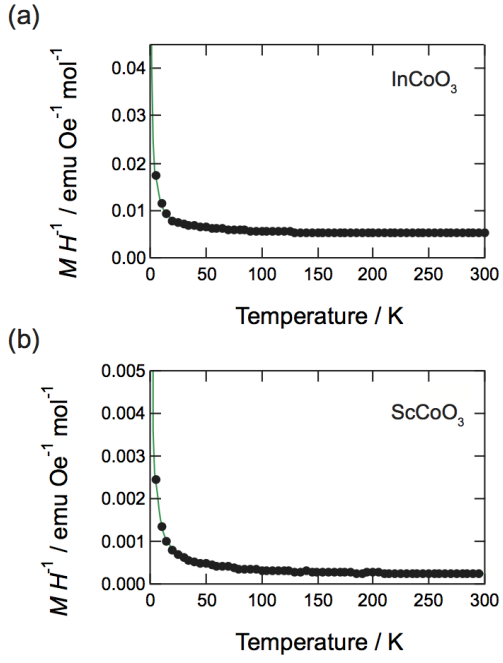


Figure 5. Temperature dependent magnetic susceptibility, χ = M/H, of (a) $InCoO_3$ and (b) $ScCoO_3$ measured at H = 100 Oe after zero-field cooling. The solid green curves represent the Curie-Weiss law.

4. DISCUSSION

In ABO_3 perovskites, oxygen octahedral tilts are driven by the need to compensate for underbonding caused by a reduction of *A*-site cation size. $GdFeO_3$-type orthorhombic (*Pnma*) structure ($a^-b^+a^-$ tilt system) is related to the cubic $Pm\bar{3}m$ perovskite structure by two octahedral tilt modes: one is the in-phase tilt ($a^0b^+a^0$) of the adjacent BO_6 octahedra about the cubic [010] axis (transforming like the irreducible representation M_3^+), and the other is the out-of-phase tilt ($a^-b^0a^-$) of the adjacent BO_6 octahedra about the cubic [101] axis (transforming like the irreducible representation R_4^+). Other kinds of structural distortions are also allowed by *Pnma* symmetry. In particular, antiparallel displacements of the *A*-site cations (transforming like the irreducible representations X_5^+ and R_5^+), which are equal in magnitude but in opposite directions in adjacent *A*O planes (see **Figure 2b** and **2d**), play a key role in stabilizing *Pnma* perovskites.[2,69] The *A* position (4*c* site) in *Pnma* has two free

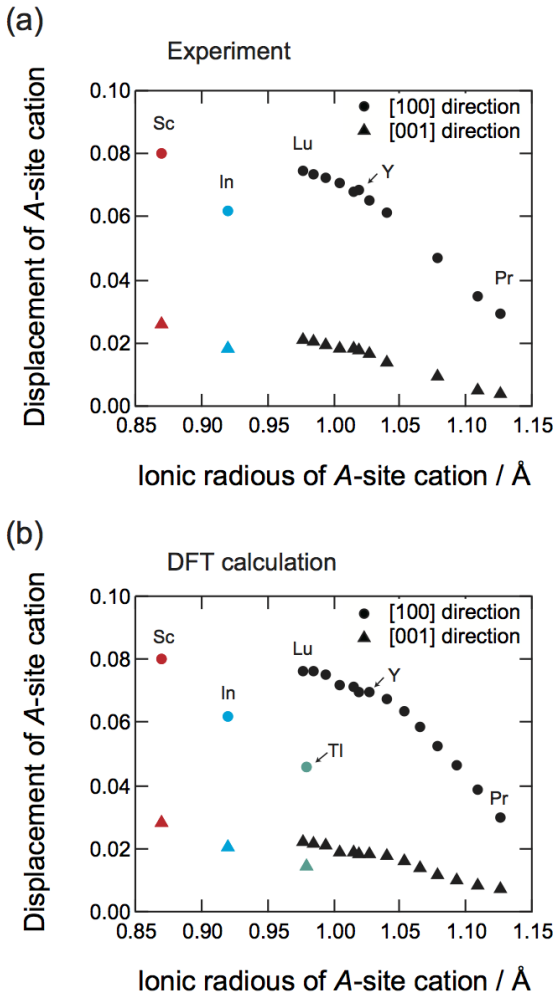


Figure 6 Variations in (a) experimental and (b) calculated *A*-site cation displacements along [100] and [001] directions (*a* and *c* directions) with A^{3+} ionic radius, r_A (in 8-fold coordination[60]) for $ScCoO_3$ (red), $InCoO_3$ (blue), and $ACoO_3$ where *A* = Y and Pr–Lu (black).[25,32–34] In (b), the calculated *A*-site cation displacements for $TlCoO_3$ (green) are shown as a reference.

parameters (x and z), thereby allowing A-site cations to shift away from their ideal $Pm\bar{3}m$ position to a more favorable coordination within the ac plane as the tilt angles are larger. Hence, the A-site coordination environment in *Pnma* perovskites is optimized by both octahedral tilts and A-site cation displacements. Given this, and the Jahn–Teller inactivity of low-spin Co^{3+} on the B-sites, the octahedral tilts and A-site cation displacements mainly affect the crystal metrics of orthocobaltites.

In light of the bonding requirements of A-site cations in *Pnma*, we discuss the origin of anomalies in the evolution of crystal metrics across the entire $ACoO_3$ series (**Figure 3a**). We here focus on the A-site cation displacements that occur within the ac plane. The experimental and calculated A-site cation displacements are plotted in **Figure 6a** and **6b** as a function of r_A, respectively. For the group 3 perovskite series $ACoO_3$ (A = Sc, Y, and Pr–Lu), both experiments and calculations present the expected increases in A-site cation displacements as r_A decreases. Nevertheless, $InCoO_3$ does not follow this trend; the antiparallel displacements along a and c directions, which are associated with the X_5^+ and R_5^+ modes, respectively, are smaller than the expected values from the trend for the group 3 series. We also see such anomalies for $TlCoO_3$ in the evolution of calculated A-site cation displacements with r_A (**Figure 6b**). As a result, group 13 (In and Tl) and group 3 (rare earth) ions optimize the *Pnma* A-site coordination environment in a different manner. Given the A-site bonding preference in *Pnma*, the smaller-than-expected A-site cation displacements should be linked to the unusual behavior of the in-phase (M_3^+ mode) and out-of-phase (R_4^+ mode) tilts (**Figure 4b**) and hence of the crystal metrics (**Figure 3**).

Next, we compare the electronic structures between group 3 and group 13 orthocobaltites. As a representative example, **Figure 7a** and **7b** depict the calculated total and partial density of states (DOS) for *Pnma* $InCoO_3$ and $YCoO_3$, respectively, where the A-site elements (i.e., In and Y) belong to the same period of the periodic table. In both cases, the valence band consists mainly of Co 3d and O 2p states (upper panels). The large differences in DOS are found on the A-site cations (lower panels). For $InCoO_3$, the formally unoccupied 5s state of In is located at much lower energies as compared to those of Y, consistently with the well-known fact that the effective nuclear charge increases with no accompanying increase in shielding effect. As a result, the In 5s state, which is completely empty in the ionic limit, is significantly occupied through orbital overlap with the O 2p state, forming the bottom of the valence band. This is evident in the orbital-projected DOS for the In site, which shows a large contribution from the In 5s state around –7 eV. Here, it should be noted that since the In "semicore" 4d states form a narrow band around –13 eV below the top of the valence band (**Figure S2** in the Supporting Information), they do not directly create covalent bonds with the O 2p state. To our knowledge, this is the first identification of the nature of covalent bonding for A-site In^{3+} ions in perovskite oxides, although the influence of such covalent bonding on crystal structure has been shown by the electronic structure

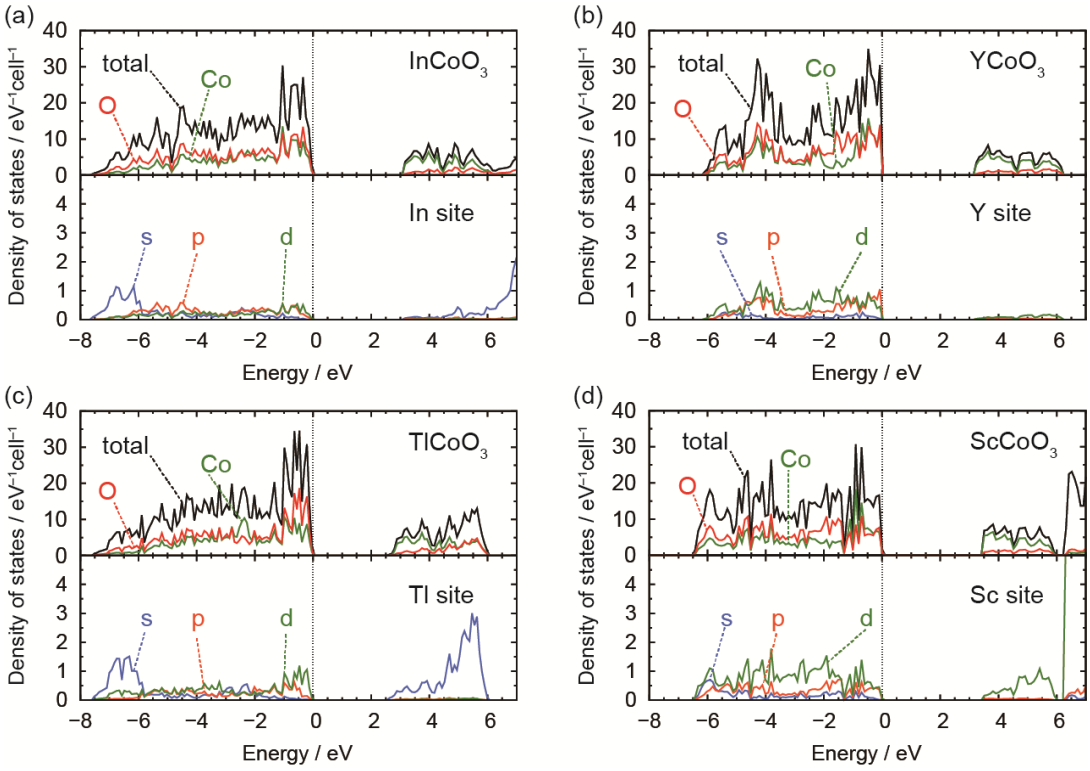


Figure 7 Calculated density of states (DOS) for diamagnetic perovskite cobaltites, (a) $InCoO_3$, (b) $YCoO_3$, (c) $TlCoO_3$, and (d) $ScCoO_3$. In each of figures, the upper panels show the total DOS and the partial DOS projected onto Co and O sites, and the lower panels correspond to the orbital-projected DOS for A-site cations. The zero of energy is set to the top of the valence band.

calculations for some nonperovskite oxides such as hexagonal $InMnO_3$.[23,70,71] For $YCoO_3$, on the other hand, the higher-lying Y 5s state has negligibly small orbital overlap with the O 2p state and so they do not contribute to the valence band. Instead, there is a small contribution from the formally empty Y 4d states through orbital overlap with the O 2p state. The difference in covalency between $InCoO_3$ and $YCoO_3$ can be also seen by comparing their valence-electron charge densities. We calculated the charge densities of the valence band electrons for $InCoO_3$ and $YCoO_3$ relative to that for $LuCoO_3$ (**Figure S3** in the Supporting Information). $InCoO_3$ shows an increase in the charge density at the outer region of the In site, accompanied by a decrease in the charge density near the O site. The high charge-density regions around the In sites extend more spatially than those around the Y sites in $YCoO_3$, reflecting the significant contribution from spherical In 5s orbitals to the covalent bond formation.

To further explore the nature of chemical bonding between *A*-site cations and oxide ions, we also carried out DFT calculations for an additional set of group 3 and 13 orthocobaltites, $TlCoO_3$ and $ScCoO_3$. The electronic structure of $TlCoO_3$ can be interpreted similarly to that of $InCoO_3$. As shown in **Figure 7c**, the Tl 6s state, although it is also formally empty in the ionic description, develop significant occupation through the overlap with the O 2p state and form the bottom of the valence band; in the orbital-projected DOS for the Tl site, a large contribution from the Tl 6s state is observed around –7 eV. Similar behavior has been identified in the electronic structure for perovskite-type $TlMnO_3$.[54] In contrast, $ScCoO_3$ behaves analogously to $YCoO_3$. As shown in **Figure 7d**, no sign of occupancy of the formally empty Sc 4s state is observed in the valence band because of its large energy gaps with the O 2p state. Our electronic structure calculations clearly indicate that group 13 (In and Tl) ions, unlike group 3 (rare earth) ions, form strong covalent bonding with oxide ions.

The orthorhombic *Pnma* distortion is the most frequently encountered structure for perovskites[72] because it allows an *A*-site cation shift and results in a better distribution of *A*−O distances.[2,69] For the group 3 series, the *A*-site coordination environment is optimized by electrostatic/ionic size mismatch effects, and hence, the smaller *A*-site cations involve the larger shifts from the ideal cubic $Pm\bar{3}m$ position (see **Figure 6**). Apart from this trend, a significant contribution from *A*–O covalent bonding exists for the group 13 series. This makes *A*-site cations reluctant to shift from their ideal position (**Figure 6)**, and thus yields a specific *A*-site coordination environment. Although the *A*-site cations are formally eight-coordinate with four nearest-neighbor and four next-nearest neighbor oxide ions, the In−O and Tl−O bonds are likely confined to the four shorter oxide ions through strong covalent bonding. The unique bonding preferences of In^{3+} and Tl^{3+} ions are responsible for the anomalies in the evolution of crystal metrics across the entire $ACoO_3$ series.

5. CONCLUSION

Two perovskite cobaltites with nearly stoichiometric composition, $InCoO_3$ and $ScCoO_3$, have been successfully synthesized via the high-pressure and high-temperature treatment at 15 GPa and 1450 ºC, although they have proved difficult to prepare. They crystallize in *Pnma* space group and exhibit large CoO_6 octahedral tilts due to the smallness of *A*-site cations (Sc^{3+} and In^{3+}). A comprehensive comparison of crystal structure for newly developed and well-known orthocobaltites $ACoO_3$ (*A* = In, Sc, Y, and Pr–Lu) highlights a distinct chemistry of $InCoO_3$ and rare earth counterparts with respect to the stabilization of *Pnma* perovskites. The peculiarity for $InCoO_3$ is caused by the *A*-site cation displacements that accompany octahedral tilts. We find, using first-principle calculations, that while the *A*-site cation displacements of rare earth series are driven by local electrostatic/ionic size mismatch effects to satisfy the *A*-site coordination requirements, there is a significant contribution from *A*–O covalency to the *A*-site optimization of $InCoO_3$, which leads to the *A*-site cation displacements smaller than expected from size mismatch effects. Both *Pnma* $InCoO_3$ and $ScCoO_3$ have a diamagnetic ground state, and will stimulate further experimental and theoretical investigations of the thermally induced spin-state transitions and possibly coupled structural and electrical properties.

6. ASSOCIATED CONTENT

Supporting Information

The Supporting Information is available free of charge on the ACS Publications website at DOI: XXXX.

Crystallographic data (CIF format), and the detailed results of SXRD data and electronic structure calculations.

7. AUTHOR INFORMATION

Corresponding Author

*Email: fujita@dipole7.kuic.kyoto-u.ac.jp (K. F.)

Author Contributions

All authors have given approval to the final version of the manuscript.

Funding Sources

This work was financially supported by JSPS KAKENHI Grant-in-Aids for Scientific Research (A) (Grant No. 25249090) and (B) (Grant No. 16H04496), Challenging Exploratory Research (Grant No. 16K14386), Scientific Research on Innovative Areas “Nano Informatics” (Grant No. 26106514), and JSPS Fellows (Grant No. 15J08052).

8. ACKNOWLEDGEMENT

High-pressure synthesis was partly supported by the Joint Usage/Research Center PRIUS, Ehime University. SXRD experiments were performed on BL02B2 at SPring-8 with the approval of JASRI (Proposal Nos. 2014A1683, 2014B1726, and 2016A1308). TOF NPD experiments at WISH were supported by a beam time allocation from STFC (RB1410149).

REFERENCES

(1) Belik, A. A.; Yi, W. High-Pressure Synthesis, Crystal Chemistry and Physics of Perovskites with Small Cations at the A Site. *J. Phys.: Condens. Matter* **2014**, *26*, 163201.

(2) Benedek, N. A.; Fennie, C. J. Why Are There So Few Perovskite Ferroelectrics? *J. Phys. Chem. C* **2013**, *117*, 13339–13349.

(3) Giaquinta, D. M.; zur Loye, H.-C. Structural Predictions in the ABO_3 Phase Diagram. *Chem. Mater*. **1994**, *6*, 365–372.

(4) Goldschmidt V. M. Die Gesetze der Krystallochemie. *Naturwissenschaften* **1926**, *14* 477–485.

(5) Li, C.; Soh, K. C. K.; Wu, P. Formability of ABO_3 Perovskites. *J. Alloys Compd*. **2004**, *372*, 40–48

(6) Castillo-Martinez, E.; Bieringer, M.; Shafi, S. P.; Cranswick, L. M. D.; Alario-Franco, M. A. Highly Stable Cooperative Distortion in a Weak Jahn–Teller d^2 Cation: Perovskite-Type $ScVO_3$ Obtained by High-Pressure and High-Temperature Transformation from Bixbyite. *J. Am. Chem. Soc.* **2011**, *133*, 8552–8563.

(7) Belik, A. A.; Matsushita, Y.; Tanaka, M.; Takayama-Muromachi, E. Crystal Structures and Properties of Perovskites $ScCrO_3$ and $InCrO_3$ with Small Ions at the A Site. *Chem. Mater.* **2012**, *24*, 2197–2203.

(8) Ding, L.; Manuel, P.; Khalyavin, D. D.; Orlandi, F.; Kumagai, Y.; Oba, F.; Yi, W.; Belik, A. A. Unusual Magnetic Structure of the High-Pressure Synthesized Perovskites $ACrO_3$ (A = Sc, In, Tl). *Phys. Rev. B: Condens. Matter Mater. Phys.* **2017**, *95*, 054432.

(9) Shannon, R. D. Synthesis of Some New Perovskites Containing Indium and Thallium. *Inorg. Chem.* **1967**, *6*, 1474–1478.

(10) Park, J. H.; Parise, J. B. High Pressure Synthesis of a New Chromite, $ScCrO_3$. *Mater. Res. Bull*. **1997**, *32*, 1617–1624.

(11) Chen, H. Y.; Yu, T.; Gao, P.; Bai, J. M.; Tao, J.; Tyson, T. A.; Wang, L.; Lalancette, R. Synthesis and Structure of Perovskite $ScMnO_3$. *Inorg. Chem.* **2013**, *52*, 9692–9697.

(12) Belik, A. A.; Matsushita, Y.; Tanaka, M.; Takayama-Muromachi, E. $(In_{1-y}Mn_y)MnO_3$ ($1/9 \leq y \leq 1/3$): Unusual Perovskites with Unusual Properties. *Angew. Chem., Int. Ed*. **2010**, *49*, 7723–7727.

(13) Belik, A. A.; Furubayashi, T.; Matsushita, Y.; Tanaka, M.; Hishita, S.; Takayama-Muromachi, E. *Angew. Chem., Int. Ed*. **2009**, *48*, 6117−6120.

(14) Belik, A. A.; Furubayashi, T.; Yusa, H.; Takayama-Muromachi, E. Indium-Based Perovskites: A New Class of Near-Room-Temperature Multiferroics. *J. Am. Chem. Soc*. **2011**, *133*, 9405–9412.

(15) Kawamoto, T.; Fujita, K.; Yamada, I.; Matoba, T.; Kim, S. J.; Gao, P.; Pan, X.; Findlay, S. D.; Tassel, C.; Kageyama, H.; Studer, A. J.; Hester, J.; Irifune, T.; Akamatsu, H.; Tanaka, K. Room-Temperature Polar Ferromagnet $ScFeO_3$ Transformed from a High-Pressure Orthorhombic Perovskite Phase. *J. Am. Chem. Soc*. **2014**, *136*, 15291–15299.

(16) Fujita, K.; Kawamoto, T.; Yamada, I.; Hernandez, O.; Hayashi, N.; Akamatsu, H.; Lafargue-Dit-Hauret, W.; Rocquefelte, X.; Fukuzumi, M.; Manuel, P.; Studer, A. J.; Knee, C. S.; Tanaka, K. $LiNbO_3$-Type $InFeO_3$: Room-Temperature Polar Magnet without Second-Order Jahn–Teller Active Ions. *Chem. Mater*. **2016**, *28*, 6644–6655.

(17) Yi, W.; Presniakov, I. A.; Sobolev, A. V.; Glazkova, Y. S.; Matsushita, Y.; Tanaka, M.; Kosuda, K.; Tsujimoto, Y.; Yamaura, K.; Belik, A. A. Structure and Cation Distribution in Perovskites with Small Cations at the A Site: the case of $ScCoO_3$. *Sci. Technol. Adv. Mater*. **2015**, *16*, 024801.

(18) Belik, A. A.; Matsushita, Y.; Tanaka, M.; Takayama-Muromachi, E. High-Pressure Synthesis, Crystal Structures, and Properties of $ScRhO_3$ and $InRhO_3$ Perovskites. *Inorg. Chem.* **2013**, *52*, 12005–12011.

(19) Yi, W.; Liang, Q.; Matsushita, Y.; Tanaka, M.; Belik, A. A. High-Pressure Synthesis, Crystal Structure, and Properties of In_2NiMnO_6 with Antiferromagnetic Order and Field-Induced Phase Transition. *Inorg. Chem.* **2013**, *52*, 14108–14115.

(20) Yi, W.; Princep, A. J.; Guo, Y.; Johnson, R. D.; Khalyavin, D.; Manuel, P.; Senyshyn, A.; Presniakov, I. A.; Sobolev, A. V.; Matsushita, Y.; Tanaka, M.; Belik, A. A.; Boothroyd, A. T. Sc_2NiMnO_6: A Double-Perovskite with a Magnetodielectric Response Driven by Multiple Magnetic Orders. *Inorg. Chem.* **2015**, 54, 8012–8021.

(21) Chris I. Thomas, Matthew R. Suchomel, Giap V. Duong, Andrew M. Fogg, John B. Claridge, Matthew J. Rosseinsky, Structure and Magnetism of the A Site Scandium Perovskite $(Sc_{0.94}Mn_{0.06})Mn_{0.65}Ni_{0.35}O_3$ Synthesized at High Pressure. *Phil. Trans. R. Soc. A* 2014, 372, 20130012.

(22) Uusi-Esko, K.; Malm, J.; Imamura, N.; Yamauchi, H.; Karppinen, M. Characterization of $RMnO_3$ (R = Sc, Y, Dy-Lu): High-Pressure Synthesized Metastable Perovskites and Their Hexagonal Precursor Phases. *Mater. Chem. Phys.* **2008**, *112*, 1029–1034.

(23) Kumagai, Y.; Belik, A. A.; Lilienblum, M.; Leo, N.; Fiebig, M.; Spaldin, N. A. Observation of Persistent Centrosymmetricity in the Hexagonal Manganite Family. *Phys. Rev. B: Condens. Matter Mater. Phys.* **2012**, *85*, 174422.

(24) Belik, A. A.; Kamba, S.; Savinov, M.; Nuzhnyy, D.; Tachibana, M.; Takayama-Muromachi, E.; Goian, V. Magnetic and Dielectric Properties of Hexagonal $InMnO_3$. *Phys. Rev. B: Condens. Matter Mater. Phys.* **2009**, *79*, 054411.

(25) Alonso, J. A.; Martínez-Lope, M. J.; De La Calle, C.; Pomjakushin, V. Preparation and Structural Study from Neutron Diffraction Data of $RCoO_3$ (R = Pr, Tb, Dy, Ho, Er, Tm, Yb, Lu) Perovskites. *J. Mater. Chem.* **2006**, *16*, 1555–1560.

(26) Raccah, P. M.; Goodenough, J. B. First-Order Localized-Electron ⇆ Collective-Electron Transition in $LaCoO_3$. *Phys. Rev*. **1967**, *155*, 932–945.

(27) Demazeau, G.; Pouchard, M.; Hagenmuller, P. Sur de Nouveaux Composés Oxygénés du Cobalt +III Dérivés de la Perovskite. *J. Solid State Chem*. **1974**, *9*, 202–209.

(28) Yan, J.-Q.; Zhou, J.-S.; Goodenough, J. B. Bond-Length Fluctuations and the Spin-State Transition in $LCoO_3$. *Phys. Rev. B: Condens. Matter Mater. Phys.* **2004**, *69*, 134409.

(29) Baier, J.; Jodlauk, S.; Kriener, M.; Reichl, A.; Zobel, C.; Kierspel, H.; Freimuth, A.; Lorenz, T. Spin-State Transition and Metal-Insulator Transition in $La_{1-x}Eu_xCoO_3$. *Phys. Rev. B: Condens. Matter Mater. Phys.* **2005**, *71*, 014443.

(30) Yamaguchi S.; Okimoto Y.; Tokura Y. Bandwidth Dependence of Insulator-Metal Transitions in Perovskite Cobalt Oxides. *Phys. Rev. B: Condens. Matter Mater. Phys.* **1996**, *54*, R11022–R11025.

(31) Stølen, S.; Grønvold, F.; Brinks, H.; Atake, T.; Mori, H. Energetics of the Spin Transition in $LaCoO_3$. *Phys. Rev. B: Condens. Matter Mater. Phys.* **1997**, *55*, 14103–14106.

(32) Tachibana, M.; Yoshida, T.; Kawaji, H.; Atake, T.; Takayama-Muromachi, E. Evolution of Electronic States in $RCoO_3$ (R = Rare Earth): Heat Capacity Measurements. *Phys. Rev. B: Condens. Matter Mater. Phys.* **2008**, *77*, 094402.

(33) Knížek, K.; Hejtmánek, J.; Jirák, Z.; Tomeš, P.; Henry, P.; André, G. Neutron Diffraction and Heat Capacity Studies of $PrCoO_3$ and $NdCoO_3$. *Phys. Rev. B: Condens. Matter Mater. Phys.* **2009**, *79*, 034103.

(34) Knížek, K.; Jirák, Z.; Hejtmánek, J.; Veverka, M.; Maryško, M.; Hauback, B. C.; Fjellvåg, H. Structure and Physical Properties of $YCoO_3$ at Temperatures up to 1000 K. *Phys. Rev. B: Condens. Matter Mater. Phys.* **2006**, *73*, 214443.

(35) Chapon, L. C.;Manuel, P.; Radaelli, P. G.; Benson, C.; Perrott, L.; Ansell, S.; Rhodes, N. J.; Raspino, D.; Duxbury, D.; Spill, E.; Norris, J. The New Powder and Single Crystal Magnetic Diffractometer on the Second Target Station. *Neutron News* **2011**, *22*, 22−25.

(36) Rietveld, H. M. Profile Refinement Method for Nuclear and Magnetic Structures. *J. Appl. Crystallogr.* **1969**, *2*, 65−71.

(37) Rodríguez-Carvajal, J. Recent Advances in Magnetic Structure Determination by Neutron Powder Diffraction. *Phys. B* **1993**, *192*, 55−69.

(38) Ida, T. Efficiency in the Calculation of Absorption Corrections for Cylinders. *J. Appl. Crystallogr.* **2010**, *43*, 1124−1125.

(39) Momma, K.; Izumi, F. *VESTA* 3 for Three-Dimensional Visualization of Crystal, Volumetric and Morphology Data. *J. Appl. Crystallogr.* **2011**, *44*, 1272−1276.

(40) Blöchl, P. E. Projector Augmented-Wave Method. *Phys. Rev. B: Condens. Matter Mater. Phys.* **1994**, *50*, 17953–11979.

(41) Kresse, G.; Hafner, J. *Ab Initio* Molecular Dynamics for Open-Shell Transition Metals. *Phys. Rev. B: Condens. Matter Mater. Phys.* **1993**, *48*, 13115–13188.

(42) Kresse, G.; Furthmüller, J. Efficient Iterative Schemes for *Ab Initio* Total-Energy Calculations Using a Plane-Wave Basis Set. *Phys. Rev. B: Condens. Matter Mater. Phys.* **1996**, *54*, 11169–11186.

(43) Kresse, G.; Joubert, D. From Ultrasoft Pseudopotentials to the Projector Augmented-Wave Method. *Phys. Rev. B: Condens. Matter Mater. Phys.* **1999**, *59*, 1758–1775.

(44) Paier, J.; Marsman, M.; Hummer, K.; Kresse, G.; Gerber, I. C.; Angyan, J. G. Screened Hybrid Density Functionals Applied to Solids. *J. Chem. Phys.* **2006**, *124*, 154709.

(45) Paier, J.; Marsman, M.; Hummer, K.; Kresse, G.; Gerber, I. C.; Angyan, J. G. Screened Hybrid Density Functionals Applied to Solids. *J. Chem. Phys.* **2006**, *125*, 249901.

(46) Heyd, J.; Scuseria, G. E.; Ernzerhof, M. Hybrid Functionals Based on a Screened Coulomb Potential. *J. Chem. Phys.* **2003**, *118*, 8207–8215.

(47) Heyd, J.; Scuseria, G. E.; Ernzerhof, M. Erratum: Hybrid Functionals Based on a Screened Coulomb Potential [J. Chem. Phys.118, 8207 (2003)]. *J. Chem. Phys.* **2006**, *124*, 219906.

(48) Krukau, A. V.; Vydrov, O. A.; Izmaylov, A. F.; Scuseria, G. E. Influence of the Exchange Screening Parameter on the Performance of Screened Hybrid Functionals. *J. Chem. Phys.* **2006**, *125*, 224106.

(49) Stroppa, A.; Marsman, M.; Kresse, G.; Picozzi, S. The Multiferroic Phase of $DyFeO_3$: an *Ab Initio* Study. *New J. Phys.* **2010**, *12*, 093026.

(50) Hong, J.; Stroppa, A.; Iniguez, J.; Picozzi, S.; Vanderbilt, D. Spin-Phonon Coupling Effects in Transition-Metal Perovskites: A DFT + U and Hybrid-Functional Study. *Phys. Rev. B: Condens. Matter Mater. Phys.* **2012**, *85*, 054417.

(51) Akamatsu, H.; Kumagai, Y.; Oba, F.; Fujita, K.; Murakami, H.; Tanaka, K.; Tanaka, I. Antiferromagnetic Superexchange via 3d States of Titanium in $EuTiO_3$ as Seen from Hybrid Hartree-Fock Density Functional Calculations. *Phys. Rev. B: Condens. Matter Mater. Phys.* **2011**, *83*, 214421.

(52) Akamatsu, H.; Kumagai, Y.; Oba, F.; Fujita, K.; Tanaka, K.; Tanaka, I. Strong Spin-Lattice Coupling Through Oxygen Octahedral Rotation in Divalent Europium Perovskites. *Adv. Funct. Mater.* **2013**, *23*, 1864−1872.

(53) Kumagai, Y.; Soda, Y.; Oba, F.; Seko, A.; Tanaka, I. First-Principles Calculations of the Phase Diagrams and Band Gaps in $CuInSe_2$-$CuGaSe_2$ and $CuInSe_2$-$CuAlSe_2$ Pseudobinary Systems. *Phys. Rev. B: Condens. Matter Mater. Phys.* **2012**, *85*, 033203.

(54) Yi, W.; Kumagai, Y.; Spaldin, N. A.; Matsushita, Y.; Sato, A.; Presniakov, I. A.; Sobolev, A. V.; Glazkova, Y. S.; Belik, A. A. Perovskite-Structure $TlMnO_3$: A New Manganite with New Properties. *Inorg. Chem.* **2014**, *53*, 9800−9808.

(55) Monkhorst H. J.; Pack, J. D. Special Points for Brillouin-Zone Integrations. *Phys. Rev. B: Condens. Matter Mater. Phys.* **1976**, *13*, 5188–5192.

(56) Glazer, A. M. The Classification of Tilted Octahedra in Perovskites. *Acta Crystallogr. Sect. B: Struct. Sci.* **1972**, *28*, 3384–3392.

(57) Brown, I. D.; Altermatt, D. Bond-Valence Parameters Obtained from a Systematic Analysis of the Inorganic Crystal Structure Database. *Acta Crystallogr., Sect. B: Struct. Sci.* **1985**, *41*, 244−247. In this work, BVS was calculated using the following parameters: b_0 = 0.37 for all atoms, r_0 = 1.902 for In, and r_0 = 1.70 for Co.

(58) Alonso, J. A.; Martínez-Lope, M. J.; Casais, M. T.; Fernández-Díaz, M. T. Evolution of the Jahn–Teller Distortion of MnO_6 Octahedra in $RMnO_3$ Perovskites (R = Pr, Nd, Dy, Tb, Ho, Er, Y): A Neutron Diffraction Study. *Inorg. Chem.* **2000**, *39*, 917−923.

(59) Sinclair, W.; Eggleton, R. A.; Ringwood, A. E. Crystal Synthesis and Structure Refinement of High-Pressure $ScAlO_3$ Perovskite. *Z. Kristallogr.* **1979**, *149*, 307.

(60) Shannon, R. D. Revised Effective Ionic Radii and Systematic Studies of Interatomie Distances in Halides and Chaleogenides. *Acta Crystallogr., Sect. A: Cryst. Phys., Diffr., Theor. Gen. Crystallogr.* **1976**, *32*, 751−767.

(61) Liu, X.; Prewitt, C. T. High-Temperature Diffraction Study of $LnCoO_3$ Perovskites: A High-Order Electronic Phase Transition. *J. Phys. Chem. Solids* **1991**, *52*, 441–448.

(62) Mitchell, R. H. *Perovskites: Modern and Ancient*, Almaz Press; Ontario, Canada, 2002.

(63) Lacorre, P.; Torrance, J. B.; Pannetier, J.; Nazzal, A. I.; Wang, P. W.; Huang, T. C. Synthesis, Crystal Structure, and Properties of Metallic $PrNiO_3$: Comparison with Metallic $NdNiO_3$ and Semiconducting $SmNiO_3$. *J. Solid State Chem.* **1991**, *91*, 225.

(64) Khattak, C.P.; Cox, D.E. Structural Studies of the (La,Sr)CrO_3 System, *Mat. Res. Bull.* **1977**, *12*, 463–471.
(65) Woodward, P. M.; Vogt, T.: Cox, D. E.; Arulraj, A.; Rao, C. N. R.; Karen, P.; Cheetham, A. K. Influence of Cation Size on the Structural Features of $Ln_{1/2}A_{1/2}MnO_3$ Perovskites at Room Temperature. *Chem. Mater.* **1998**, *10*, 3652-3665.
(66) Kennedy, B. J.; Howard, C. J.; Chakoumakos, B. C. Phase Transitions in Perovskite at Elevated Temperatures –A Powder Neutron Diffraction Study. *J. Phys.: Condens. Matter* **1999**, *11*, 1479–1488.
(67) Yi, W.; Matsushita, Y.; Katsuya, Y.; Yamaura, K.; Tsujimoto, Y.; Presniakov, I. A.; Sobolev, A. V.; Glazkova, Y. S.; Lekina, Y. O.; Tsujii, N.; Nimori, S.; Takehana, K.; Imanaka, Y.; Belik, A. A. High-Pressure Synthesis Crystal Structure and Magnetic Properties of $TlCrO_3$ Perovskite. *Dalton Trans.* **2015**, *44*, 10785−10794.
(68) Kim, S. J.; Demazeau, G.; Presniakov, I.; Choy, J. H. Structural Distortion and Chemical Bonding in $TlFeO_3$: Comparison with *A*FeO_3 (*A* = Rare Earth). *J. Solid State Chem.* **2001**, *161*, 197−204.
(69) Woodward, P. M. Octahedral Tilting in Perovskites. II. Structure Stabilizing Forces. *Acta. Crystallogr. Sect. B: Struct. Sci.* **1997**, *53*, 44–66.
(70) Zhang, Y. G.;Wang, Y. X. Density-Functional Study of the Electronic Structure and Optical Properties of Transparent Conducting Oxides $In_4Sn_3O_{12}$ and $In_4Ge_3O_{12}$. *J. Electron. Mater.* **2011**, *40*, 1501–1505.
(71) Mryasov, O. N.; Freeman, A. J. Electronic Band Structure of Indium Tin Oxide and Criteria for Transparent Conducting Behavior. *Phys. Rev. B: Condens. Matter Mater. Phys.* **2001**, *64*, 233111.
(72) Lufaso, M. W.; Woodward, P. M. Prediction of the Crystal Structures of Perovskites Using the Software Program SPuDS. *Acta. Crystallogr. Sect. B: Struct. Sci.* **2001**, *57*, 725–738.